



Instrument Science Report WFC3 2013-10

In-flight Corrections to the WFC3 UVIS Flat Fields

J. Mack, E. Sabbi, & T. Dahlen

June 25, 2013

ABSTRACT

Improved flat fields for the entire set of 42 full frame UVIS filters were ingested into the HST archive on December 14, 2011. These new reference files typically improve the accuracy of point source photometry by 0.6 to 1.8% (rms), with maximum differences of ~3 to 6% depending on filter. The flat fields in use prior to this date were obtained from ground test data and contained a set of four internal window reflections affecting ~45% of the detector field of view, with a typical 0.5-2.0% effect on photometry. A simplified geometric model was used to remove this artifact from the flat fields. Additional low-frequency residuals, caused by differences in the ground and in-flight optical paths, were then computed using relative photometry of bright stars in Omega Centauri measured at multiple positions across the detector. These calibration data have been used to study the UVIS PSF in more detail, and for aperture radii smaller than 0.4" (10 pixels) the encircled energy is found to vary strongly with detector position. The photometric response for any given star using the revised flat fields is accurate to $\pm 1\%$ over the detector for most UVIS filters. Flat fields for the 4 bluest UV filters were obtained 'warm' (-49C versus -82C) during ground testing, and these show $\pm 2-3\%$ residuals in a 'crosshatch' pattern across the detector. Several calibration programs are underway to model and correct this residual flat field structure. For sources with SED's significantly different than the average Omega Centauri population, color terms of up to a few percent may be present.

Introduction

In the final thermal vacuum test (TV3, spring 2008), the Wide Field Camera 3 (WFC3) team carried out a complete set of calibrations for the reduction of on-orbit data. At that time, a full set of flat field reference files was obtained by simulating the sky illumination of the UVIS CCDs using the CASTLE optical stimulus (Sabbi et al. 2009). These flat

fields include both a high-spatial frequency component that accounts for pixel-to-pixel variations in response (P-flat) and a low-spatial frequency component (L-flat) that corrects for large-scale modulations across the detector.

Initial on-orbit testing during Servicing Mission Observatory Verification (SMOV) showed that the flats derived from ground test data did not fully remove low- and mid-frequency structures. In program 11452 (UVIS Flat Field Uniformity, PI: Quijano), differences of ~1.5 to 4.5% were found in a subset of 6 filters using observations of two galactic globular clusters (Sabbi 2009). Since that time, additional calibration data has been obtained in Cycles 17 and 18 (programs 11911 & 12339, “UVIS L-flats”, PI: Sabbi), in a key set of 10 broadband filters used most frequently by observers. These new data have been used to further characterize the on-orbit response of the instrument.

To generate the new UVIS flat fields, the ground flats were modified to include two significant corrections: the removal of a large-scale internal reflection (or ‘flare’) and a residual correction for low-frequency (L-flat) differences in the ground and in-flight optical paths. A geometric model was used to predict the shape and brightness of the flare (McCullough 2011), and the remaining low-frequency residual structures were derived from high signal-to-noise observations of stars in Omega Centauri. By placing the same stars over different portions of the detector and measuring relative changes in brightness, local variations in response have been computed. The same methodology and software developed for the ACS L-flats (van der Marel 2003) has been used for this work. ‘Flare-free’ versions of the ground flats were multiplied by the filter-dependent L-flat corrections to create improved versions of the flat reference files used in the WFC3 calibration pipeline (CALWF3).

For the first ~2.5 years of operation, all UVIS science data downloaded from the HST archive were calibrated using the original ground test flat fields. On August 8, 2011, revised flat fields were delivered for 7 broadband filters (F336W, F390W, F438W, F555W, F606W, F775W, F814W). The intent of this preliminary delivery was to allow users to make use of the improved calibrations, while the flats for other filters were being investigated. The remaining 35 UVIS filters (excluding the ‘quad’ filters) were delivered on December 14, 2011 to complete the full set of 42 full-frame flats. These included the final 3 broadband filters from the L-flat calibration program (F225W, F275W, F850LP) plus the remaining 32 UVIS filters for which the L-flat correction was computed via interpolation based on the filter pivot wavelengths.

Because the overall flat field calibration involved a number of separate smaller studies, the work will be presented in a series of ISRs. This first ISR will provide an overview of the steps required to correct the ground flats. It will focus on solutions obtained for 10 broadband filters and will discuss several methods used to validate the accuracy of the solutions. The second ISR (Dahlen et al. 2013) will describe the method for interpolating the solutions for the remaining 32 UVIS filters and the expected accuracy of the interpolated flats. The third ISR (Sabbi & Bellini 2013) will quantify variations in the encircled energy of the PSF, both spatially (across the detector) and temporally (throughout the orbit).

1. Terminology

The WFC3 flat fields have been constructed using a variety of different methods, from data obtained on the ground and in flight. The following terminology is defined for reference:

- LP- FLAT : map of the instrument response, including both low spatial frequency (L) and pixel-to-pixel (P) variations in sensitivity.
 - ✓ **Ground flat**: Obtained during TV3 by illuminating the detector with the CASTLE optical stimulus. These flats map the wavelength-dependent, high spatial frequency information about the uniformity of the detector. They generally require low-frequency corrections to account for differences in the simulator versus the true on-orbit illumination. For the UVIS detector, these flats also contain a large-scale internal reflection or “flare”.
 - ✓ **Internal flat**: Obtained in flight using the internal calibration subsystem. These are used to monitor time variability in the pixel-to-pixel (P) response and track populations of deviant pixels as the detector ages. These are not used directly in the calibration pipeline primarily because their illumination pattern is quite different than that of the Optical Telescope Assembly (OTA).
 - ✓ **Earth flat**: Obtained in flight from observations of the sunlit or moonlit Earth. These often contain scattered light or cloud streaks, especially at visible wavelengths, making them difficult to use as reference files.
 - ✓ **Sky flat**: Obtained in flight from many co-added observations of sparse fields with astronomical sources (stars, galaxies, etc) masked out.
- L- FLAT : low-frequency correction to the ground flats, computed in flight using:
 - ✓ **Stars**: Residuals are derived by stepping stars across the detector and measuring relative changes in photometry. The mathematical algorithm used in this study to compute L-flat residuals is described in Section 5.
 - ✓ **Earth**: Residuals are computed by flat fielding an Earth flat with the ground flat.
 - ✓ **Sky**: Residuals are computed from co-added observations of sparse fields with sources masked. When the signal-to-noise ratio of an HST sky flat is not adequate to model the pixel-to-pixel instrument response, sky flats may be smoothed and used to map low- and mid-frequency residuals to the ground flats. This strategy was used to correct the WFC3 IR flats (Pirzkal et al. 2011), referred to as sky ‘delta’ flats. The authors note that the flats were ‘de-noised’ by Fourier filtering. As such, these flats could be considered a

hybrid between ‘delta’ flats and L-flats since they correct low and mid-frequency structure. Sky flats have not been explored for the UVIS detector due to the lower sky background levels at shorter wavelengths, requiring many exposures to build up a flat of sufficient signal-to-noise.

- DELTA FLAT : changes in the pixel-to-pixel instrument response, computed in flight. These are not currently used for WFC3, but could be generated using internal flats to correct pixels with anomalous sensitivity variations between anneals. For details, see programs 12808 (PI Pavlovsky) and 13169 (PI Gunning). Delta flats could also be generated from very high signal-to-noise (unsmoothed) sky flats.

Flats fields provide a map the total instrument response and represent the combined throughput of several individual components. The SYNPHOT software package may be used as a dynamic throughput generator to:

- ✓ list the components for a unique observation mode (task= ‘showfiles’)
- ✓ generate total system throughput curves (task= ‘calcband’)
- ✓ compute photometric keywords ‘on the fly’ (task= ‘bandpar’)
- ✓ predict count rates in raw or flat fielded data (task= ‘calcphot’).

Table 1 list the ten throughput curves describing a flat fielded F606W image on UVIS1, where observation mode = ‘camera, detector, filter, flat’ = ‘wfc3, uvis1, f606w, cal’. For more information about the use of SYNPHOT tasks with the available HST observing modes, refer to the SYNPHOT Data User’s Guide (2008).

Table 1. The SYNPHOT component tables which combine to describe a particular observation mode, in this case, flat fielded F606W images obtained with the UVIS1 detector.

--> *showfiles ‘wfc3, uvis1, f606w, cal’*

Component Table	Description
hst_ota_007_syn.fits	HST Optical Telescope Assembly throughput
wfc3_pom_001_syn.fits	WFC3 pickoff mirror reflectivity
wfc3_uvis_mir1_002_syn.fits	Reflectivity of UVIS mirror 1
wfc3_uvis_mir2_002_syn.fits	Reflectivity of UVIS mirror 2
wfc3_uvis_owin_002_syn.fits	Transmission of UVIS outer window
wfc3_uvis_iwin_002_syn.fits	Transmission of UVIS inner window
wfc3_uvis_ccd1_003_syn.fits	Raw quantum efficiency for UVIS detector chip 1
wfc3_uvis_f606w_004_syn.fits	Filter Transmission for F606W
wfc3_uvis_f606wf1_002_syn.fits	Normalization (midpoint) of F606W flat chip 1
wfc3_uvis_cor_003_syn.fits	UVIS inflight throughput correction (SMOV)

2. The Ground Flat Calibration

The UVIS channel is equipped with 47 filters and one UV grism. Of the 47 filters, 42 are full-frame filters and 5 are ‘quad’ filters consisting of four different filters covering the four detector quadrants. The L-flat correction described in this report addresses the full-frame flats only, and not the ‘quad’ filters.

During ground testing in 2008, the UVIS flat fields were acquired for all filters with a total signal of $\sim 75,000$ electrons per pixel from a stack of ~ 3 images per filter (Sabbi et al. 2009). From Poisson statistics, this would give an error of $\sim 0.37\%$ per pixel. The CASTLE optical stimulus was used to provide flat field illumination of the flight detector. Flats with xenon and halogen (QTH) lamps were taken with the detector at its expected flight temperature of -82C (IUVDETMP header keyword). A subset of ultraviolet flats was acquired at a warmer temperature (IUVDETMP= -49C) using the deuterium lamp to achieve higher count rates. Differences in the UV flat field response due to temperature were expected, and additional on-orbit calibration data is required to correct a residual ‘crosshatch’ pattern in these flats. A summary of the CASTLE stimulus and temperature is presented as a function of filter in Table 2. This new table supercedes the values given in Table 1 of Sabbi et al. (2009) for several filters.

The UVIS flat fields were normalized to unity in a 100×100 pixel box in UVIS1 amplifier A, coordinates [1032:1133,328:429]. This region was selected due to the absence of contaminants known as ‘droplets’ which are mineral residue on the outer window of the flight detector (Brown et al. 2008). Because the sensitivity varies over UVIS1, the median flat field value for this chip will be close to, but not exactly equal to 1.0. UVIS2 was divided by the same normalization value as UVIS1 to preserve the relative sensitivity difference between the two CCDs. Unlike the ACS/WFC detector, the two UVIS chips were not cut from the same silicon wafer and as such are two independent detectors. As a result, the median flat field value for UVIS2 may be significantly lower than 1.0, especially in the UV, where the UVIS2 detector achieves higher sensitivity than UVIS1. Because the QE differences are accounted for during flat fielding, users need only apply a single zeropoint value when performing photometry from both chips using calibrated flat fielded (flt.fits) or drizzled (drz.fits) images.

Because the WFC3 focal plane is tilted with respect to the incoming beam, the projected pixel area on the sky varies across the field of view in calibrated (flt.fits) images, and therefore pixels in different regions of the detector collect a different amount of light simply due to the projected area. As a result, observations of a constant surface brightness object would have count rates per pixel that vary over the detector, even if every pixel had the same sensitivity. In order to produce images that appear uniform for uniform illumination, the LP-flat fields include the effect of the variable pixel area across the field. As a consequence of dividing by the flat field, two stars of equal brightness in an ‘flt.fits’ image falling on different portions of the detector would not have the same total counts. To correct for this effect, point source photometry extracted from ‘flt.fits’ images may be multiplied by the effective pixel area map (Kalirai et. al. 2010). Alternatively, this correction is accounted for in the pipeline by drizzling (Fruchter et al., 2002), where the

geometric distortion solution is used to correct all pixels to equal area on the sky in the ‘drz.fits’ data products.

A subsample of the UVIS flats from ground test data are presented over the broad wavelength range of the detector (Figure 1). A complete set can be found in the ‘UVIS CASTLE Photometric Filter Flat Field Atlas’ (Sabbi, 2008). Notable features in the flat fields include the following:

- A crosshatch pattern at bluer wavelengths due to structure in the detection-layer. This pattern almost entirely disappears at wavelengths greater than ~500 nm.
- A large, diffuse dark spot at the bottom of amplifier D for wavelengths greater than ~600nm. The strength of this feature increases with wavelength and is due to variations in the silicon detector layer thickness (Figure 2, adapted from Wong 2010), which affect the sensitivity.
- Vertical striping, similar to piano keys in the broadband longpass filters, particularly F850LP, but also F200LP, F350LP, and F600LP. At wavelengths approaching ~1 micron, which these longpass filters probe, the detector becomes transparent and the piano key pattern is due to the glue adhesive on the other side of the CCD.
- Fringing: position- and wavelength-dependent patterns in brightness caused when internal reflections within the detector lead to interference patterns. Narrow band filters redder than ~600nm are affected by fringing (Wong 2010). Figure 1 illustrates the fringe pattern for the F952N filter.

In addition to these filter-specific features, a large wedge-shaped ‘flare’ is present in the full set of flat fields. This artifact is due to an internal reflection between the detector and the four surfaces of the UVIS inner and outer windows and is especially noticeable in the F606W flat field. The flare and methods to remove it from the ground flats are discussed in Section 6.

Table 2. CASTLE ground flat stimulus and temperature for the UVIS full-frame flats.

Lamp	Temp	UVIS Filter
Deuterium	-49C	F218W, F225W, F275W, F280N
Xenon	-82C	F200LP, F300X, F336W, F343N, F350LP, F373N, F390M, F390W, F395N, F410M, F438W, F467M, F469N, F475W, F475X, F487N, F502N, F547M, F555W, F600LP, F631N, F645N, F656N, F657N, F658N, F665N, F673N
Halogen(QTH)	-82C	F606W, F621M, F625W, F680N, F689M, F763N, F775W, F814W, F845M, F850LP, F953N

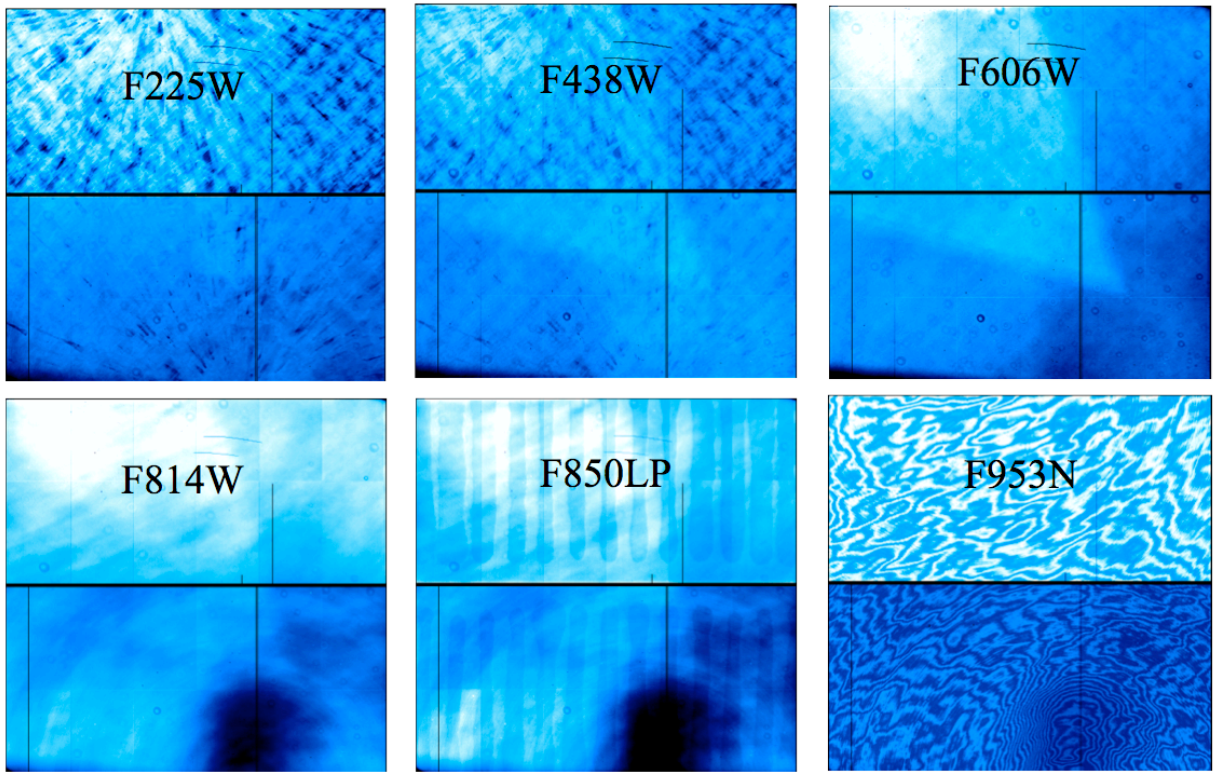


Figure 1: A subset of CASTLE flat fields obtained during Thermal Vacuum Testing. STIMULUS = D_2 ($\lambda < 300$ nm), Xe ($300 \text{ nm} < \lambda < 531 \text{ nm}$), Xe or QTH ($\lambda > 600$ nm). Dark regions correspond to lower response pixels in the LP-flats.

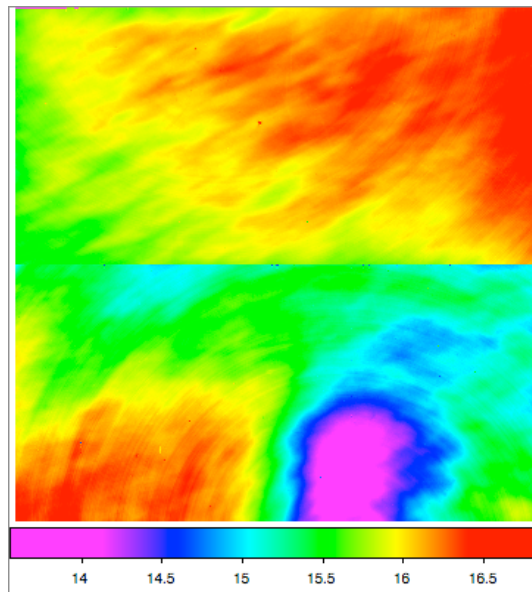


Figure 2: UVIS detector layer thickness in microns (Wong 2010).

3. Star Cluster Observations

Due to differences in the HST optical path, any flat fields acquired in flight were expected to differ from those obtained during ground testing. Neither the laboratory flat field illumination nor the on-orbit internal lamp flats provide an accurate simulation of the OTA. For this reason, low-frequency residuals in the spatial response (L-flat) were characterized by observing a dense star field with multiple telescope orientations and large dithered steps across the detector.

Omega Centauri was selected as a calibration target due to its rich population of stars, including hot (blue) horizontal branch and cold red giant stars. The core of the cluster is very extended (~ 2.5 arcmin) and lacks a strong stellar density gradient, making it an ideal region for computing relative differences in photometry as a function of detector position. To obtain an adequate characterization of the flat field stability, 9 pointings were obtained for each filter using a 3x3 box dither pattern. These included dither steps of 40" (approximately 25% of the FOV) in either the x and/or y direction, as shown in Figure 3. The chosen pattern allows an independent measurement of the detector charge transfer efficiency since dithers along the y-axis have been included.

Observations were obtained in 10 UVIS filters most frequently selected by GOs as of Cycle 17: F225W, F275W, F336W, F390W, F438W, F555W, F606W, F775W, F814W, F850LP. The broad wavelength range covered by these observations allow the L-flat correction to be interpolated for the remaining UVIS filters. Follow-up dithered observations of the same field, obtained at additional detector orientations, were utilized for further constraining the solutions. The full set of calibration observations are summarized in Table 3. The exposure time and number of images used to generate the L-flat solutions are given in Table 4.

Table 3. WFC3/UVIS observations of Omega Centauri over multiple epochs.

Cycle	Proposal	Orbits	PI	Date	Orient (degrees)	Filters
SMOV*	11452	6	Kim-Quijano	Jul 2009	332	F225W F275W F336W
Cycle 17	11911	30	Sabbi	Jan 2010 Apr 2010 Jul 2010	150 245 325	F225W F555W F275W F606W F336W F775W F390W F814W F438W F850LP
Cycle 18	12339	14	Sabbi	Feb 2011	185	F225W F555W F275W F606W F336W F814W F438W F850LP

*These exposures were shorter than the Cycle 17 & 18 observations and were therefore not included in computing the L-flat solutions.

Figure 3: The 9 dither positions for each epoch of Omega Centauri observations can be seen in the weight image of the drizzled product. The blue box outlines the UVIS field of view for a single exposure. The calibration observations were obtained in a 3x3 grid, with dither steps of ~25% of the FOV. Note that the combined weight image is shown for illustration of the dither pattern only, since the individual exposures were used to compute relative photometry.

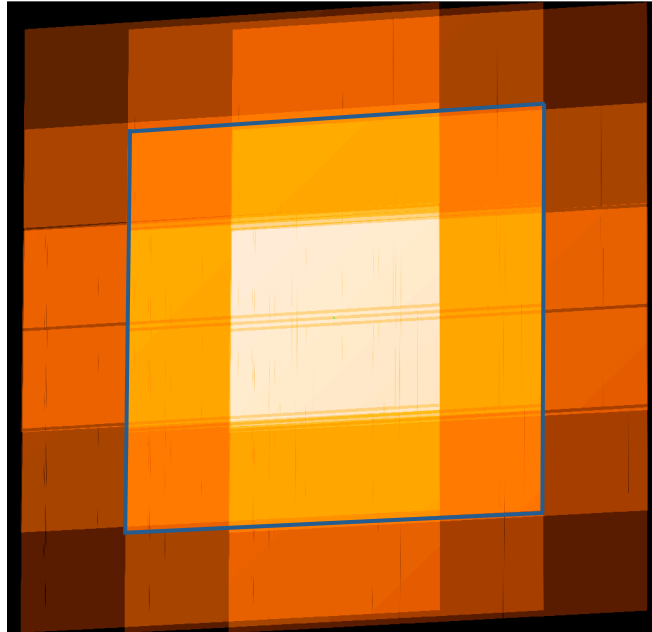


Table 4. The exposure time per image, the number of exposures, and the total exposure time used to compute the L-flat solutions from the combined Cycle 17 and 18 calibration programs.

Filter	Exptime (seconds)	Number of Observations	Total Time (seconds)
F225W	900	27	24,300
F275W	800	31	24,800
F336W	350	28	9,800
F390W	350	15	5,250
F438W	350	22	7,700
F555W	40	15	600
F606W	40	19	760
F775W	350	16	5600
F814W	40	19	760
F850LP	60	23	1,380

4. Analysis

All UVIS datasets were calibrated with CALWF3 v2.2, using the most up-to-date bias and dark reference files. CALWF3 divides by the ground flats, which correct for the relative gain between amplifiers, and then multiplies by the average gain value in the CCDTAB reference file to produce calibrated data products units of electrons. Prior to Feb 2010 (and the availability of CALWF3 v1.8.1), the amp-dependent gain values in the CCDTAB were applied to each quadrant of the science image, in the same way as done for ACS. Because the WFC3 ground flats already contained offsets between amplifiers, the resulting science images incorrectly received a double correction for the relative gain. To resolve this problem, CALWF3 was modified to apply only the average gain to all four amplifiers after the flat fielding step.

Aperture photometry was performed on the individual calibrated ‘flt.fits’ exposures with the goal of computing magnitude differences between measurements of the same stars at different positions on the detector. To correct for the effect of varying pixel area (see Section 2), each exposure was multiplied by the UVIS pixel area map. The IRAF/DAOPHOT task ‘phot’ was used to compute photometry within an aperture radius of 5 pixels and a sky annulus between $r=7$ and $r=9$ pixels. These values were chosen as a compromise between the need for large apertures to overcome variations in focus and telescope breathing, while limiting the effects of crowding for very large apertures.

Matched source catalogs were created using the software ‘xym2mat’ and ‘xym2key’ (Anderson et al. 2006). These routines look for sources in common between images using a variety of pattern-recognition tests. An iterative approach was taken, computing an initial solution from only the brightest unsaturated stars and then revising that solution using the entire catalog. The resulting source catalogs contain approximately 5000 stars per image, are matched by position across input frames, and contain only stars with no bright neighbors.

Finally, the catalogs for each image were merged into a single master catalog per filter including a unique stellar ID, the image number, the chip, the detector x/y position (not corrected for distortion), and the observed magnitude and error. This catalog contains anywhere from 3-28 measurements of each star over different portions of the detector. For illustration, a few lines of the master catalog for a given filter are shown in Table 5.

Table 5. Format of the master catalog used to compute L-flat

#	star	image	chip	xflt	yflt	mag	error
	1	1	1	3836.28	38.04	19.676	0.015
	1	3	2	3394.96	1729.89	19.697	0.016
	1	4	2	2955.27	1322.79	19.697	0.016
	1	7	1	3405.23	513.21	19.691	0.015
	1	10	1	2968.69	996.01	19.695	0.015
	2	1	1	625.32	449.06	19.404	0.012
	2	2	1	1079.20	861.28	19.427	0.013
	2	8	2	627.26	1650.38	19.434	0.013
	2	13	2	1083.08	1171.12	19.416	0.013

5. Matrix Solution Algorithm

Low-frequency corrections to the UVIS flat fields were characterized using the same software (makeLflat5) and methodology developed for ACS (van der Marel 2003). The specific analysis and resulting L-flat corrections for the three ACS detectors (WFC, HRC, and SBC) are described in a series of papers (Mack et al. 2002, Mack et al. 2005a, and Mack et al. 2005b).

The L-flat correction is an over-determined matrix equation with a minimum chi-square solution, where the optimal order of the solution is determined by the density of stars and the number of observations per star. The solutions can be represented either as a set of 2-D Legendre polynomials or as a ‘chessboard’ grid of basis functions of varying order. The solutions take the form 2^n , where the 3rd, 4th, and 5th order solutions result in an 8x8, 16x16 and 32x32 pixelated version of the UVIS detector. In the 32x32 solution, one grid ‘pixel’ corresponds to 128x128 detector pixels.

An initial set of L-flat solutions for the F606W filter is presented in Figure 4. These solutions are based on the first visit (Jan 2010) of program 11911, which contains 9 dithered images at a single orientation. Because the shape of the L-flat residuals was not yet known, both polynomial and chessboard basis function solutions were explored. One advantage of using polynomials is that cohesive structures are well represented. A disadvantage is that the solutions cannot describe intermediate frequency structures unless high order fits are used, and these can cause large excursions near the detector edges. With the chessboard basis functions, the L-flat is made up of independent solutions for each grid point. A disadvantage of this approach is that grid regions with few measurements may result in large scatter in the final grid.

The average residual of the stellar magnitude with respect to the predicted magnitude is shown in the top two rows, where positive magnitudes (light blue) indicate that the photometry obtained using the ground flats will be too faint. The 1-sigma errors associated with each solution are shown in rows 3 & 4. Note that these errors are generally larger for the chessboard basis functions since independent L-flat solutions are computed for each grid point, whereas the polynomial solutions are based on information from neighboring grid points. A map of the number of measurements per input grid pixel is shown in row 5. The dither pattern illustrated in Figure 3 can be recognized here. This map is useful for determining when too few stars per grid pixel are available to determine a reliable solution. In those cases, the L-flat solution may either be interpolated from adjacent pixels, or a lower order solution may be chosen.

The 5th order grid solution begins to resolve a large ‘wedge-shaped’ feature covering ~45% of the detector field of view. This unusual feature was later determined to be an internal reflection or ‘flare’ in the ground flat reference files (see Section 6). Because the edges of the flare are angled with respect to the detector axes, this artifact cannot be accurately removed using even the highest resolution 32x32 grid. Instead the WFC3 team used ground test calibration data to develop a geometric model of the reflection in order to remove it from the ground flats prior to computing the L-flat solutions.

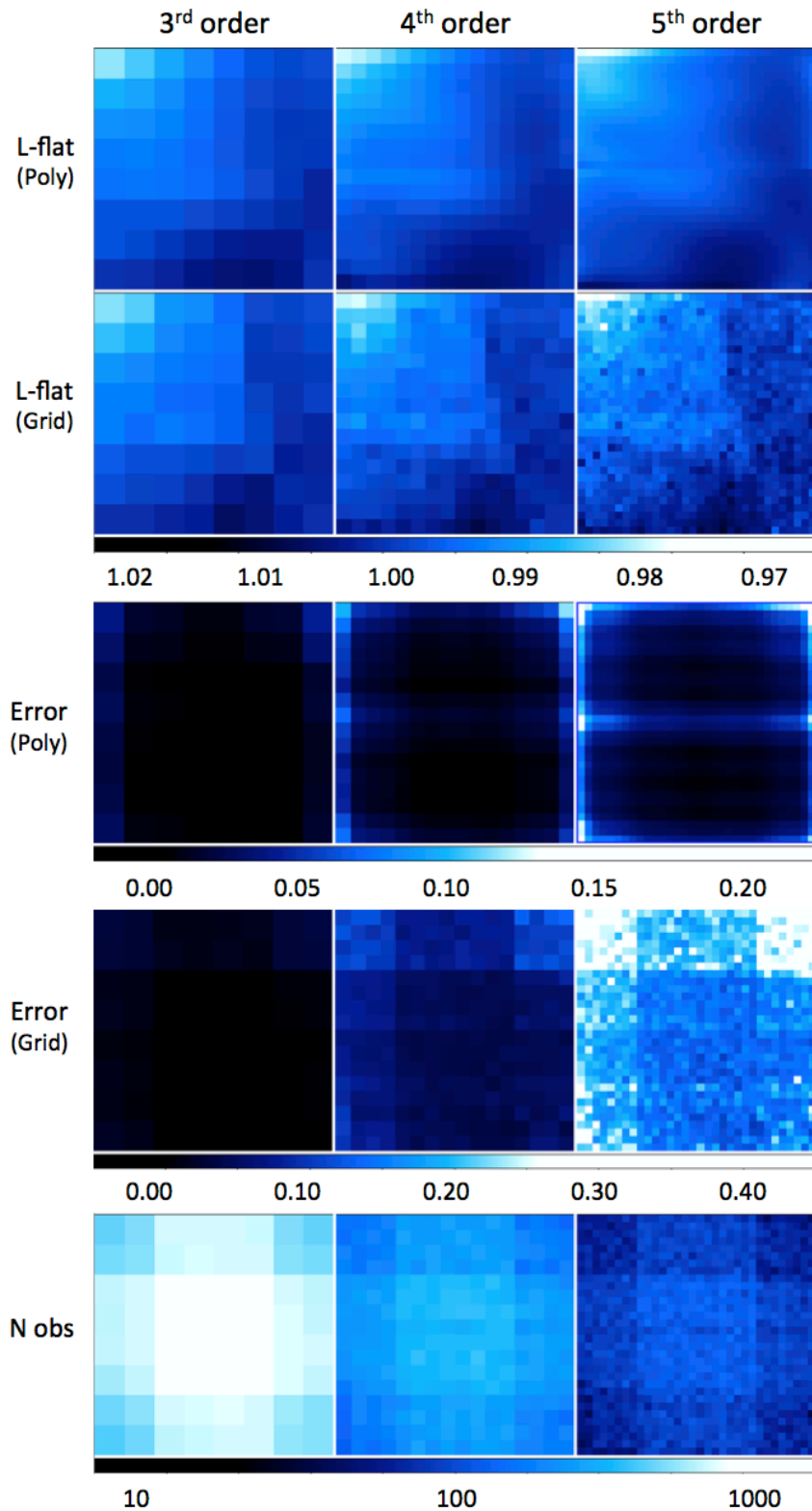


Figure 4: An initial set of L-flat solutions for F606W are presented as 2-D Legendre polynomials (row 1) and ‘chessboard’ basis functions (row 2) of varying order. The stretch is $\pm 3\%$, where light blue indicates that the ground flats overcorrect the photometry, making sources too faint. The formal 1-sigma errors associated with each solution (in percent) are shown in rows 3 & 4, along with a map of the number of observations per grid ‘pixel’ (row 5).

6. The UVIS Flare

Because of the tilted UVIS focal plane, light is reflected multiple times between the detector and the two chamber windows. Window ghosts were predicted from early models of the UVIS detector (Stiavelli et al, 2001) and were produced with an optical stimulus during ground testing (Brown & Lupie, 2004). When a point source is positioned in the lower right quadrant of the UVIS detector, out-of-focus reflections between the CCD and windows appear along a diagonal from the source towards the upper left, well removed from the source. These figure-eight shaped ghosts gradually move outside the field of view as the target moves out of the lower right corner.

An extended ‘flare’ in the ground flats was first noticed (and thus named) in a report summarizing the results of the UVIS broadband flat field testing during thermal-vacuum testing in the fall of 2004 (Bushouse 2005). In this test, external flats were obtained with the CASTLE Optical Stimulus in three filters, and the author notes a large-scale ‘flare’ running diagonally across the detector in both CCD chips at a level of 1-2%. Bushouse soon realized that the bright diamond-shaped pattern observed in the flats was a result of detector window ghosts (Brown 2007a).

On-orbit calibration data confirmed that the flare is a result of the UVIS window ghost reflections, and it is only apparent when the detector is illuminated by a uniform surface brightness source in amplifier D. In an effort to verify the accuracy of the ground flats, on-orbit flat fields were obtained by exposing the full OTA to a uniform external light source. Specifically, the dark side of the Earth was observed during periods of full moon illumination in Cycle 17 (program 11914, PI: McCullough) and Cycle 19 (program 12709, PI: Pavlovsky). Both the ground flats and the moonlit Earth flats show a bright wedge-shaped flare (Figure 5, top row). The pixelated L-flat solution derived from stellar photometry (bottom left) shows a negative imprint of this same pattern, indicating that the flare should not be part of the flat field when calibrating astronomical targets that do not fully illuminate the detector. Because flat fielding is a multiplicative correction, the Omega Centauri photometry is compromised by this internal reflection in the ground flat.

To better understand the properties of the flare, a geometric model was derived using knowledge of the relative tilt of the detector with respect to the two chamber windows (McCullough 2011). This model was generated by projecting the four defocused ellipses, or ghosts, created from each of the four internal reflections between the detector and the front and back surfaces of the two windows.

A set of TV3 calibration images were used to measure the properties of the ghost reflections, including their relative brightness with respect to the primary source. In the test, saturated exposures of a HeNe laser spot were organized in a 6x6 grid across quadrant D, creating ghost ellipses along a diagonal to the upper left (Brown 2008a). The sum of 36 images is presented in Figure 6 (left), where real data is shown in black and colored ellipses are over-plotted to guide the eye between sources and ghosts. McCullough numerically simulated the summation of the many defocused ellipses from a uniform illumination of the detector. The result (Figure 6, right) replicates the wedge-shaped ‘flare’ apparent in both the ground flats and in the on-orbit Earth flats. This model predicts the relative strength of

each of the four reflections with respect to the primary source and is useful for determining the shape and extent of each flare. The Omega Centauri L-flat residuals, on the other hand, give an initial estimate of the absolute brightness of the flare as a function of wavelength.

To remove the flare, the individual chips (extensions 1 and 4) in the LP-flat reference file were copied into a single full frame image, including the 31 pixel chip gap. Each chip was divided by the pixel area map, each amplifier corrected for its unique gain value, and the QE offset between chips removed using the relative throughput derived by SYNPHOT. To approximate the defocused edges of the flare, the model in Figure 6 was smoothed with a 240 pixel boxcar. McCullough notes that the vertex of the flare in the flat field is not precisely where it is predicted by the model, likely because the reflective silicon of the CCD extends beyond the active area that is read out as pixels. Thus, the model was shifted along the diagonal until it best matched the position of the flare in the flat.

Each ground flat was corrected by a scaled flare model, where a range of flare strengths close to the initial estimate were used to see which best removed the feature ‘by eye’. This correction takes the form $(\text{ground flat} / (1 + \text{scale} * \text{flare}))$ which for small values of $(\text{scale} * \text{flare})$ is approximately equal to $(\text{ground flat} - \text{scale} * \text{flare})$. Finally, the QE offset, gain, and pixel area map were reintroduced to create ‘flare-free’ versions of the ground flats for each test scaling factor.

The Omega Centauri data were recalibrated using CALWF3 and the new ‘flare-free’ ground flats. Aperture photometry of the cluster was recomputed, and new L-flat solutions were generated for each of the test flare strengths to verify which best removed any signature of this feature in the chessboard grid solution (either over- or under-subtracted). Note that this second approach is more robust than the ‘by eye’ scaling where it is difficult to see the flare in the ground flat, especially in the UV and far-red filters where other structures, such as the crosshatch pattern, chip thickness effects, and vertical striping, dominate the flats (see Figure 1).

The final adopted flare strengths are presented in Table 6 for each of the 10 broadband filters. The maximum correction is in the upper left corner of the detector where the sum of the four internal reflections ranges from 1.0% (in the F225W filter) to 2.4% (in F850LP filter).

Additional calibration data in Cycle 19 (program 12706, PI: Mack) will help improve our understanding of the strength of the flare as a function of wavelength, especially for the bluest filters where the flare is faint compared to other structure in the flat field. In this new program, short narrowband exposures will be used to measure the brightness of a single star, and deep saturated broadband exposures of the same star will be used to obtain high signal-to-noise measurements of each ghost to characterize the primary source to ghost ratio as a function of wavelength.

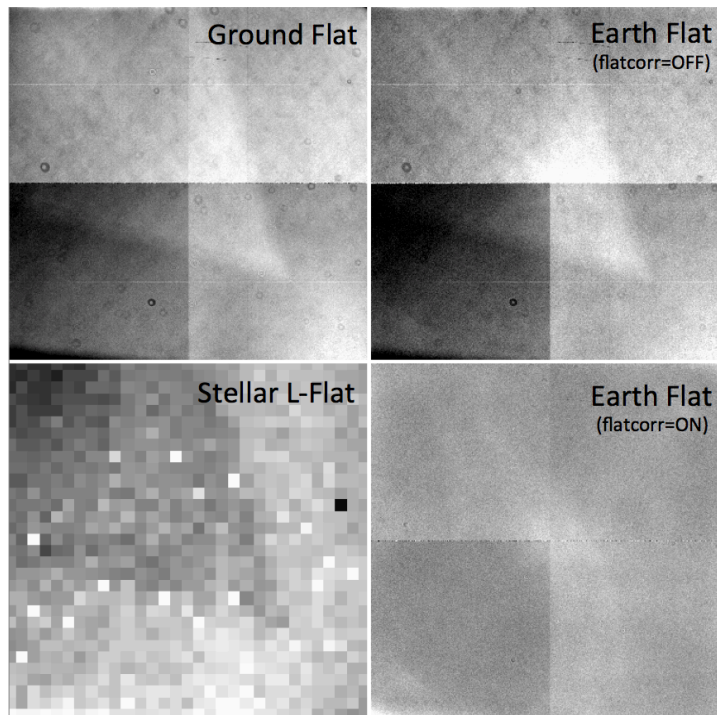


Figure 5: The F606W ground flat (top left) is strikingly similar to the in-flight Earth flat with the CALWF3 flat fielding step turned off (top right). Turning on flat fielding makes the flare feature disappear (bottom right). The L-flat correction image (bottom left) shows a negative imprint of the flare, implying that it is not a true feature of the L-flat, but instead an internal reflection in the ground flat which is imprinted on the Omega Centauri images during the flat fielding process. The image stretch ranges from 0.97 (black) to 1.03 (white).

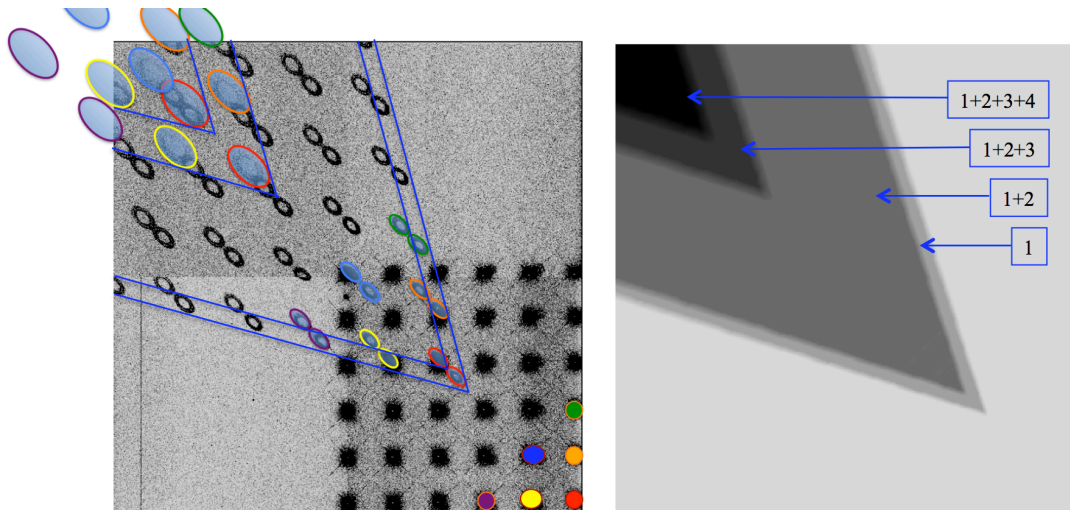


Figure 6: (Left, from McCullough 2011) Sum of 36 images obtained in TV3 where a source is moved in a 6x6 grid across amp D. Colored circles and ellipses are over-plotted to guide the eye from the source to the corresponding ghost ellipses to the upper left. A uniform surface brightness source will create a constant surface brightness ‘flare’ for each of the 4 reflections off the window surfaces. (Right) Geometric model of the sum of the 4 ghost reflections for a source which uniformly illuminates the detector.

Table 6. Strength of the flare (percent). The flare has its maximum effect in the upper left corner of the detector, where it is the sum of four separate internal reflections.

Filter	Ghost (1)	Ghosts (1+2)	Ghosts (1+2+3)	Ghosts (1+2+3+4)
F225W	0.25	0.50	0.75	1.00
F275W	0.40	0.80	1.20	1.60
F336W	0.25	0.50	0.75	1.00
F390W	0.45	0.90	1.35	1.80
F438W	0.40	0.80	1.20	1.60
F555W	0.40	0.80	1.20	1.60
F606W	0.40	0.80	1.20	1.60
F775W	0.40	0.80	1.20	1.60
F814W	0.40	0.80	1.20	1.60
F850LP	0.60	1.20	1.80	2.40

7. Encircled Energy Variations

Once the flare was removed from the ground flats, a new set of L-flat solutions were generated using the matrix algorithm. Solutions for a variety of photometric apertures were computed, and both shape and strength of the flat residuals showed variations with aperture. The dependence on aperture (and therefore encircled energy) is shown in Figure 7 for the F606W filter. The solutions become noisier with increased aperture radius, presumably due to the effects of stellar crowding.

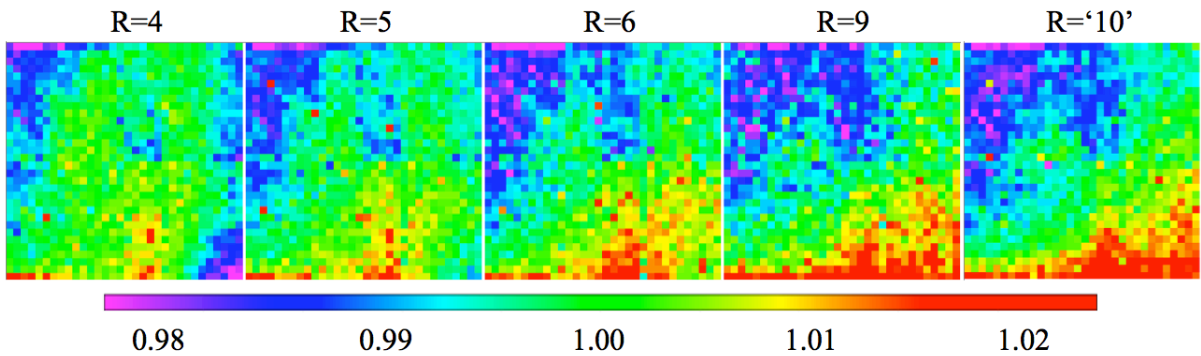


Figure 7: Low-frequency flats derived for the F606W filter from aperture photometry in a 4, 5, 6 and 9 pixel radius (shown from left to right). The far-right panel (R='10') shows the L-flat computed from photometry in a 5 pixel aperture, corrected to 10 pixels (0.4") using a spatially-dependent aperture correction.

Rather than using larger and larger apertures, an alternate approach is to use small aperture photometry but correct for spatial variability of the PSF by applying local aperture corrections. A PSF library was computed for each individual exposure using software developed by Bellini & Bedin (2009), based on algorithms developed by Anderson et al. (2006) to derive a spatially variable PSF library for undersampled images. The software was used to divide the detector into a 9x10 grid (Figure 8, left) and compute a unique PSF for each grid position based on stars contained within that region.

Using these custom PSF libraries, a set of 90 encircled energy curves were computed for each image. The aperture correction required to correct photometry to 10 pixels is shown in Figure 8 (center) as a function of aperture radius for one example F336W image. For radii smaller than 0.32'' (8 pixels), the UVIS PSF depends strongly on detector position. Beyond 8 pixels, the aperture correction to 10 pixels is less than 1% over the entire detector. The PSF is extremely stable beyond 0.4'' (10 pixels). For illustration, the aperture correction map from R=5 to 10 pixels (Figure 8, right) is presented for the example image.

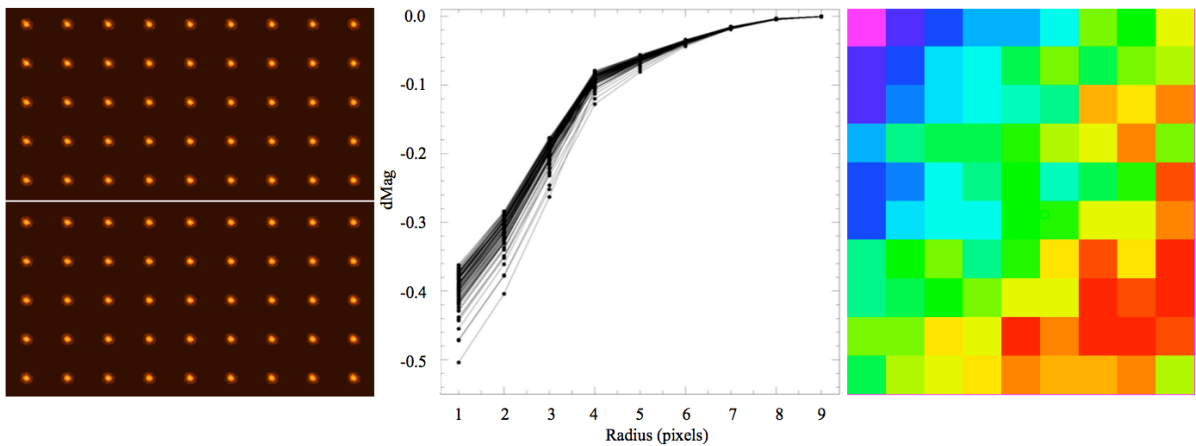


Figure 8: (Left) 9x10 PSF library for one example F336W image, derived using software from Bellini & Bedin (2009). (Center) Aperture correction to 10 pixels (delta mag) versus radius for all 90 PSFs, where R=1 represents the aperture correction from 1 to 10 pixels. The total correction is less than 1% beyond 8 pixels. (Right) Aperture correction map from R=5 to R=10 pixels, with a range of -0.073 mag (purple) to -0.041 mag (red). Note that this map changes slightly from one exposure to the next as the PSF samples different parts of the HST breathing curve.

In addition to spatial variations, telescope breathing can also impact the PSF, and therefore the L-flat solutions, if not properly corrected. This is especially important in the upper left portion of the UVIS detector. Variations in the computed aperture correction as a function of orbital position are shown in Figure 9 for five F336W images of Omega Centauri acquired in sequence. The total correction from R=5 to 10 pixels ranges across the field of view from -0.073 mag (purple) to -0.041 mag (red), where the maximum difference for any given position is ~0.008 mag.

The focus position at the time of each observation (MJD) was derived from the HST Focus Model (<http://www.stsci.edu/hst/observatory/focus/FocusModel>) which estimates the amount of defocus (in microns) at a particular HST camera. In the lower-left panel, the

focus is plotted at 5 minute intervals for a period of several hours to show the time variability. The time range corresponding to the consecutive F336W observations is over-plotted in red. The lower-right panel shows a decline of ~ 0.003 mag in the median aperture correction for the sequence of images. For more details about PSF variations on the timescale of an HST orbit, Figure 11 in Dressel (2012) plots the relation between the telescope focus and the encircled energy for several apertures.

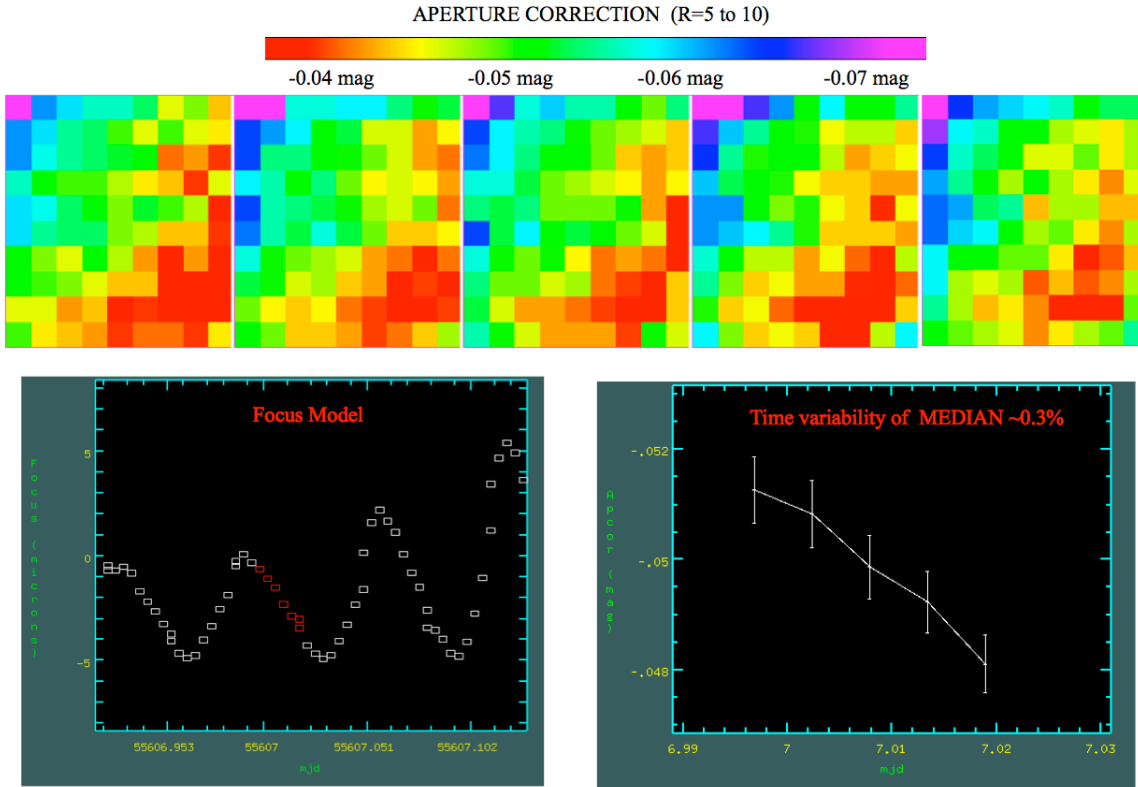


Figure 9: (Top) The R=5 to R=10 pixel aperture correction for five consecutive images obtained in the F336W filter. A model of the telescope focus in microns is plotted as a function of time (lower left), and the time range of the five consecutive observations is shown in red. The lower-right panel plots the median aperture correction and the standard deviation for the five sequential images.

Prior to applying this encircled energy correction, an ‘alpha’ release of the corrected flat fields for 7 filters (F336W, F438W, F555W, F606W, F775W, F814W) was posted to the WFC3 webpage on March 25, 2011. These initial solutions combined the flare-corrected ground flats with the residual low-frequency corrections to produce new versions of the LP-flat reference files, and they reduced the flat field errors from $\sim 5\%$ to $\sim 1\%$.

To verify the accuracy of the ‘alpha’ flats, a calibration program in Cycle 17 (proposal 12090, PI: Kalirai) was designed to test the spatial repeatability of the photometry by stepping a white dwarf spectrophotometric standard, GD153, in a regular grid across the detector using the F336W filter. Photometry was performed using a 10 pixel aperture

radius, and the results showed clear spatial variability, where a star positioned in the bottom right corner of the detector was $\sim 2\%$ fainter than when it was placed in the top left corner (Rajan et al. 2013, in preparation). This is shown in the left panel of Figure 10, where the percent variation with respect to the mean is plotted.

This early result led to a more thorough investigation of the spatial dependence of the PSF and whether the observed residuals could be due to the different aperture size used for the stepped star analysis ($r=10$ pixels) compared to the L-flat study ($r=5$ pixels). Indeed, once the Omega Centauri aperture photometry was corrected to 10 pixels and new L-flats computed, the systematic residuals seen in the stepped standard star photometry disappear (Figure 10, right).

The far-right panel of Figure 7 (labeled $R= '10'$) gives the L-flat solution obtained using photometry in a 5 pixel aperture combined with a local aperture correction from 5 to 10 pixels. The $R= '10'$ solution is significantly different than the $R=5$ solution but nearly identical to the $R=9$ solution (albeit with less noise), validating the robustness of the technique. More details on the UVIS PSF and its spatial variability will be presented in a forthcoming ISR (Sabbi & Bellini 2013, in preparation).

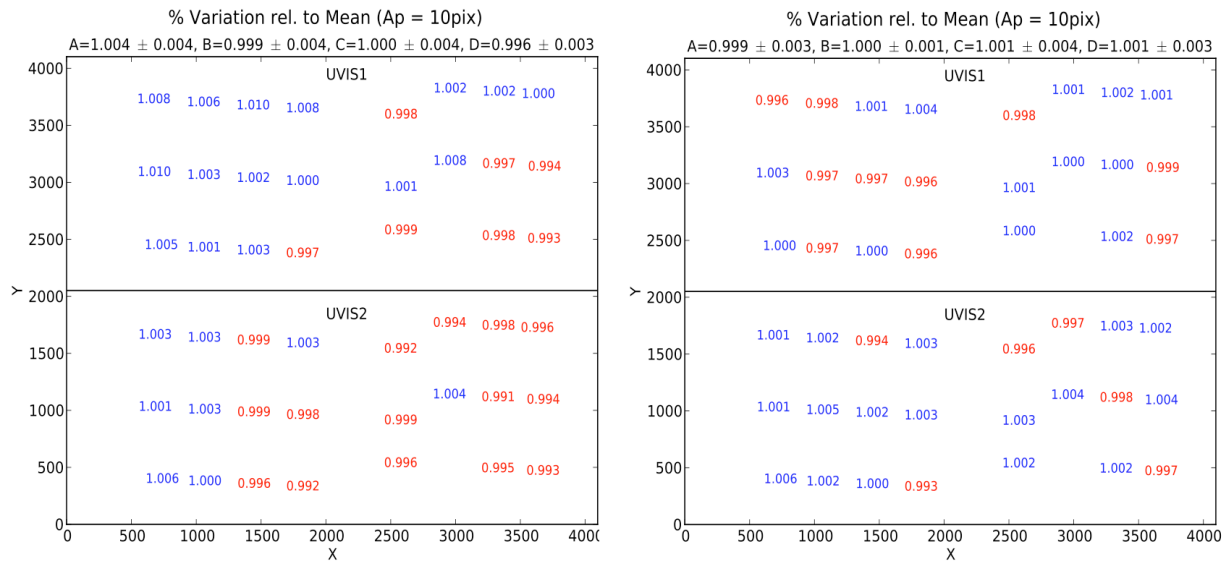


Figure 10: Percent variation relative to the mean for the white dwarf standard GD153 stepped over the frame in the F336W filter (Rajan et al. 2013). Photometry computed in a 10 pixel aperture using the ‘alpha release’ flats shows systematic residuals across the detector (left panel). When using the revised flat fields, which were derived from aperture photometry corrected to 10 pixels, the spatial residuals disappear (right panel). To guide the eye, values less than 1.0 are shown in red, values greater than or equal to 1.0 in blue. The mean and associated error for each amplifier are given at the top of each plot.

8. The L-flat solutions

The L-flat solutions represent the ratio of detector illumination between ground and in-flight observations. To create these solutions, multiple exposures of Omega Centauri were obtained at a range of orientations and with large dithered steps, allowing us to sample the same stars at different locations across the detector field of view. Aperture photometry was performed with a radius of 0.2'' (5 pixels) to minimize uncertainties due to crowding. The images were flat-fielded by a modified version of the TV3 flat fields obtained during ground testing, corrected for a 'flare' caused by an internal reflection between the detector and the two window surfaces. A spatially variable aperture correction to 0.4'' (10 pixels) was applied to the photometry computed for each image to account for variations in the PSF due to detector position and telescope focus (including both breathing and long term focus trends).

The 10 broadband L-flat solutions are presented in Figure 11. These represent the pixelized 'grid' solutions generated by the matrix solution algorithm. With the exception of the two bluest UV flats, which were obtained under ambient conditions during ground testing, the sensitivity residuals show a general wavelength dependence, where the required correction deviates from unity more at longer wavelengths compared to shorter ones.

For the majority of filters, solutions were derived using a 32x32 grid (5th order). The exceptions are the bluest F225W and F275W filters and the reddest F850LP filter for which a 16x16 grid (4th order) was used. Lower order solutions were used for the UV filters due to lack of a sufficient number of blue stars in the cluster to create an accurate solution over the entire pixelized grid. For F850LP, the detector becomes transparent at ~1 micron so that the glue adhering the detector to its package becomes visible. The sensitivity in these glue bands is dependent on the color of the source, and the 5th order L-flat solution is biased by these glue features. These two special cases (the UV and the far-red) are discussed further in Section 11.

A map of the number of measurements per output grid pixel is presented in Figure 12 for one 4th order and one 5th order solution, represented by F275W and F606W. Note that fewer measurements are available in the corners of the detector due to the dithering scheme (Figure 3), and the L-flats in these regions will have slightly larger uncertainties.

The L-flat is by definition intended to model only low-frequency sensitivity variations and therefore cannot be exactly reproduced by the adopted pixelized basis functions. The accuracy of these solutions can therefore be improved through the application of additional smoothing (van der Marel, 2003). First, deviant pixels in the grid solutions (those differing by more than 3-sigma from their neighbors) were replaced with the mean value from the neighboring pixels. Next, the pixelized solutions were resampled back to the full-size detector. The L-flats were then smoothed using a 2-D gaussian with a dispersion equal to one grid pixel ($\sigma_x=\sigma_y=1$), corresponding to 256 and 128 detector pixels for the 4th and 5th order solutions.

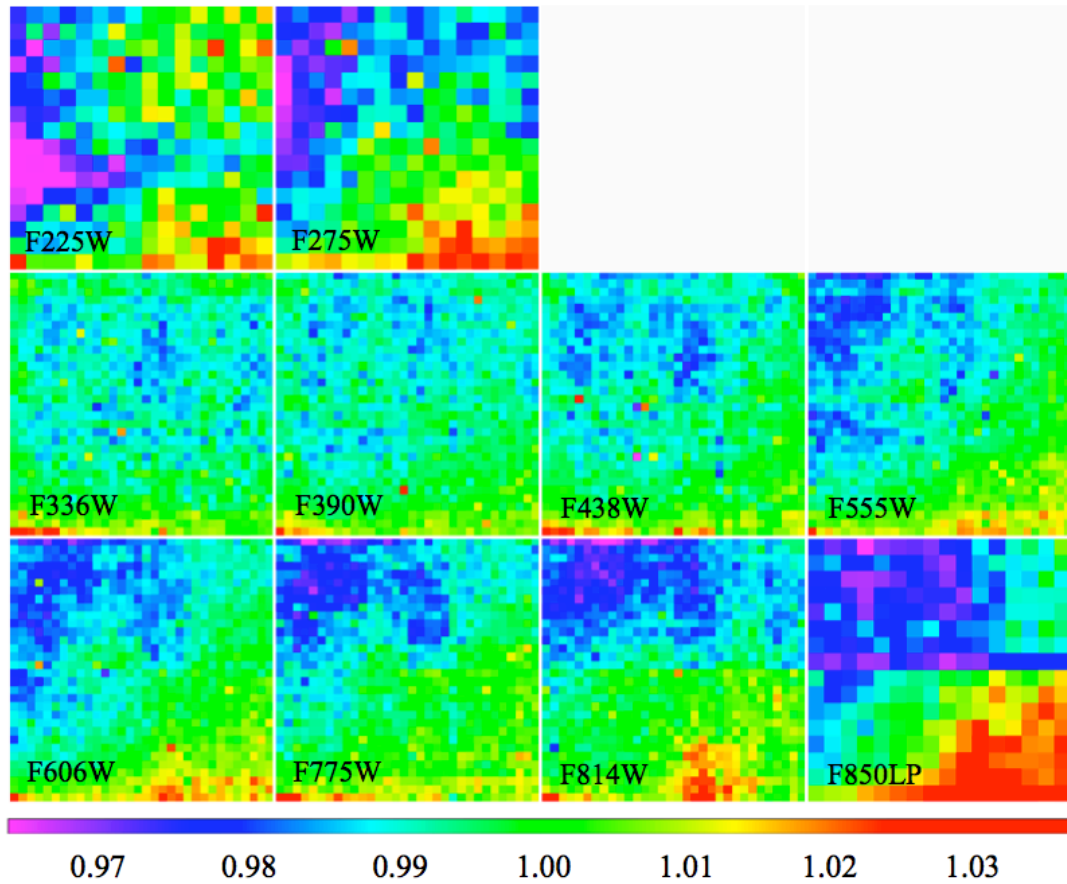


Figure 11: Low-frequency corrections to the ground LP-flats (flare removed). Blue indicates that the flare-corrected ground flats overcorrect the data, making the photometry too faint. The solutions are presented as a 32x32 grid for most broadband filters, such that one grid pixel corresponds to 128x128 detector pixels. The exceptions are F225W, F275W, and F850LP for which 16x16 grid solutions were used, where one grid pixel corresponds to 256x256 detector pixels.

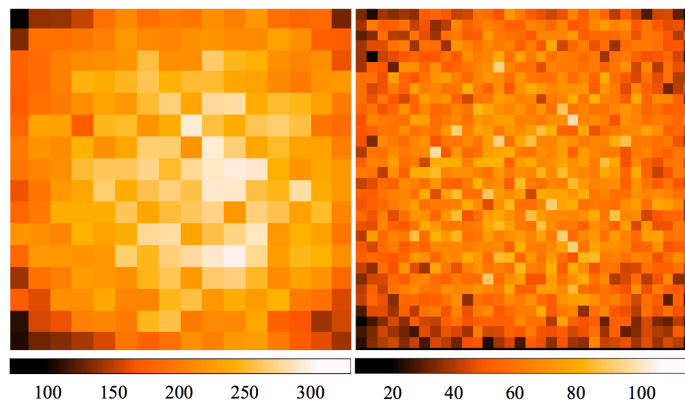


Figure 12: Number of measurements per grid 'pixel' for the 4th and 5th order solutions in representative filters F275W and F606W.

9. Pipeline Reference Files

To create the revised in-flight LP-flats for use in the pipeline, the flare-subtracted ground flats were multiplied by the smoothed L-flat solutions for each chip. The flat fields were then normalized to unity using the same 100x100 pixel box in amplifier A selected for the ground flat normalization (see Section 2). UVIS2 has been divided by the same normalization value as UVIS1 to preserve the overall sensitivity difference between the CCDs such that only a single zeropoint need be applied to the calibrated data.

CALWF3 supports up to three separate flat-field reference files: a pixel-to-pixel flat field (PFLTFILE), a low-frequency flat field (LFLTFILE), and a delta flat field (DFLTFILE) containing any needed changes to the small-scale PFLTFILE. If the LFLTFILE and DFLTFILE are not specified in the image header, only the PFLTFILE is used for the flat-field correction. If two or more reference files are specified, they are read in line-by-line and multiplied together to form a combined flat-field correction image.

Rather than carrying a separate L-flat reference file, which would be combined with the ground flat during the flat fielding step, the new reference files are revised LP-flats, created by dividing the existing ground flats (corrected for the flare) by the new L-flat corrections. The ratio of the revised pipeline flats with respect to the original ground flats is presented in Figure 13 for the 10 broadband filters in this study. The new reference files are different from the ground flats by 0.6 to 1.8% rms, with a maximum change of ~ 2.8 to 5.5%, depending on filter (see Table 7).

For the remaining 32 UVIS filters, the residual flat field correction was computed via interpolation based on the filter pivot wavelength. The general wavelength dependence of both the flare correction and the L-flat solutions suggests that interpolation is a valid method for generating these reference files. (Dahlen et al. 2013, in preparation).

Because of strong variability in the UVIS encircled energy, users are advised to apply local aperture corrections when computing aperture photometry with radii smaller than 0.4" (10 pixels). The PSF is stable beyond this radius, and the UVIS photometric zeropoints (Kalirai et al. 2009) were therefore computed for the 0.4" aperture, as well as for an infinite aperture. Note that the zeropoint calibration observations were conducted using 512x512 subarrays in the corners of amplifiers A and C. Unfortunately, the amplifier A observations fall on the strongest part of the UVIS flare, where the ground flats contain the sum of four internal detector-window reflections. With the availability of new flatfields, the UVIS zeropoints were therefore recomputed and delivered to SYNPHOT in March 2012 for incorporation in the image headers by CALWF3. These new calibration results were also posted to the WFC3 Photometric Zeropoints webpage: http://www.stsci.edu/hst/wfc3/phot_zp_lbn. Changes in the 2012 zeropoints were less than 2% for most filters.

Figure 13: Ratio of the revised pipeline flats to the original ground flats. Blue indicates that the ground flats overcorrect the data, making sources too faint.

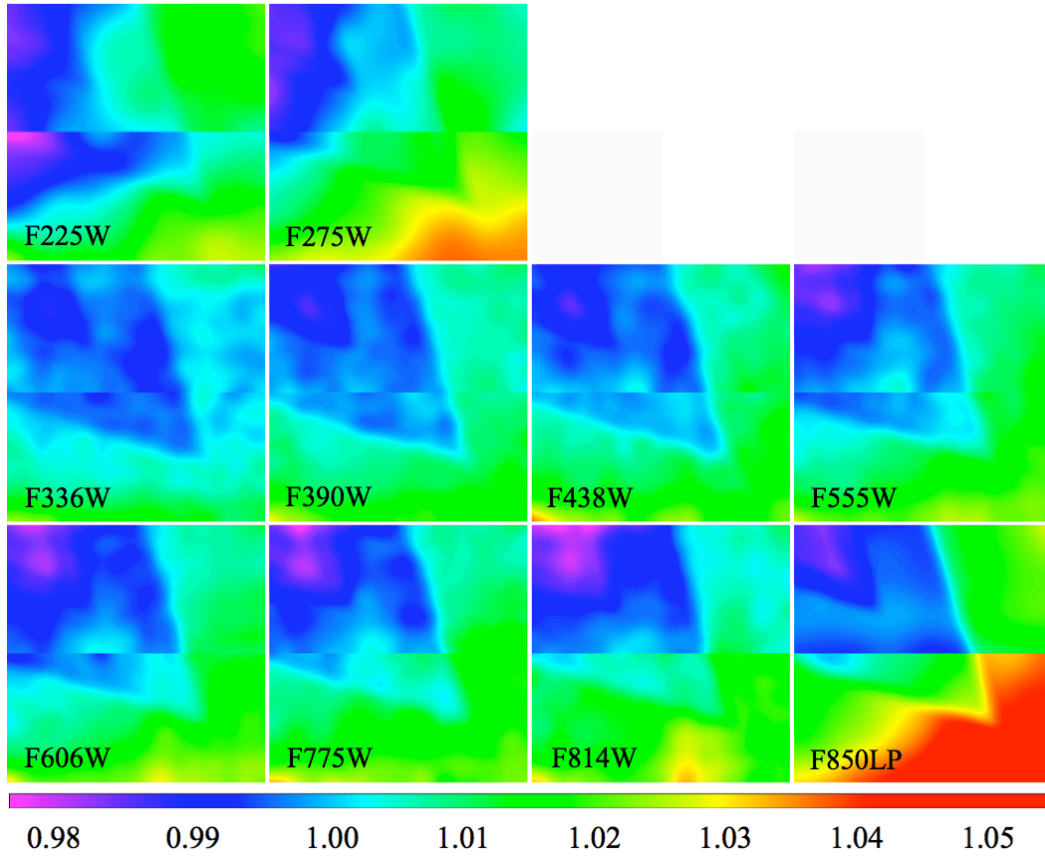


Table 7. The typical and maximum change in photometry as a function of filter, based on statistics of the flat field ratio images in Figure 13.

Filter	RMS (%)	Maximum (%)
F225W	0.011	0.028
F275W	0.013	0.039
F336W	0.006	0.027
F390W	0.008	0.032
F438W	0.008	0.038
F555W	0.010	0.030
F606W	0.010	0.034
F775W	0.010	0.035
F814W	0.012	0.035
F850LP	0.018	0.055

10. Validation of the Solutions

The L-flat solutions have been independently generated using aperture photometry in calibrated ‘flt.fits’ images (corrected for varying pixel area) and in drizzled (‘drz.fits’) images, where the filter-specific geometric distortion correction was applied by MultiDrizzle. By making use of the world coordinate system in the header of each image, MultiDrizzle applies the necessary rotation, shift, and scale required to align images. It also ‘blurs’ the PSF slightly by resampling the pixels onto an output grid and then convolving with a specific drizzling kernel. Photometry obtained after resampling the images is less ideal for deriving corrections to the flat field reference files which are applied in the calibration pipeline *prior* to drizzling. As a validation check, however, L-flats were computed using both types of images to verify that the two methods gave consistent solutions.

Once the new LP-flats were created, the full set of Omega Centauri data were recalibrated and aperture photometry recomputed. To verify that no systematic residuals remained, a ‘second iteration L-flat’ was created for each filter. As expected, these showed deviations of less than 1% with no spatial dependence.

To assess the photometric accuracy of data calibrated with the new flats, the difference in apparent magnitude for stars found in two F814W images acquired 5 months apart (~185 degree roll) is presented in Figure 14. Only stars with estimated photometric errors less than 0.1% are included in the plot. The relative magnitude is plotted as a function of the x-position for four separate regions selected by the y-position. The separate panels were created from 5 pixel aperture photometry using the ground flat (left), the March 2011 ‘alpha release’ flat (center) and the new pipeline flat with local aperture corrections to 0.4" (right).

Relative photometry using the ground flats shows large spatial residuals (rms=0.025 mag), especially for $x < 2000$ pix and $y > 3000$ pix, where the flare is strongest and for $y < 1000$ pix and $x \sim 3000$ pix where the silicon detector layer is the thinnest. Photometry obtained with the ‘alpha release’ flats and the new flats are nearly identical, with rms residuals of ~0.010 mag. The similarity in the residuals is not surprising, since the ‘alpha release’ flats were specifically designed to work for a 5 pixel aperture. While the alpha version of the flat fields was accurate only for photometry with a 5 pixel aperture, the new flats can be applied to any dataset, as long as the photometry is corrected to an 0.4" aperture.

Further validation of the new flats comes from the Cycle 17 calibration data described in Section 7, where a spectrophotometric standard was stepped across the detector in F336W to assess the spatial repeatability (Rajan et al. 2013, in preparation). Systematic residuals apparent in Figure 10 using the ‘alpha release’ flat disappear when using the revised pipeline flat, where the average variation with respect to the mean for the 46 individual measurements is 1.000 ± 0.003 . Note that the sole difference between the ‘alpha’ flat and the revised flat is the application of a spatially dependent aperture correction prior to computing the L-flat solutions.

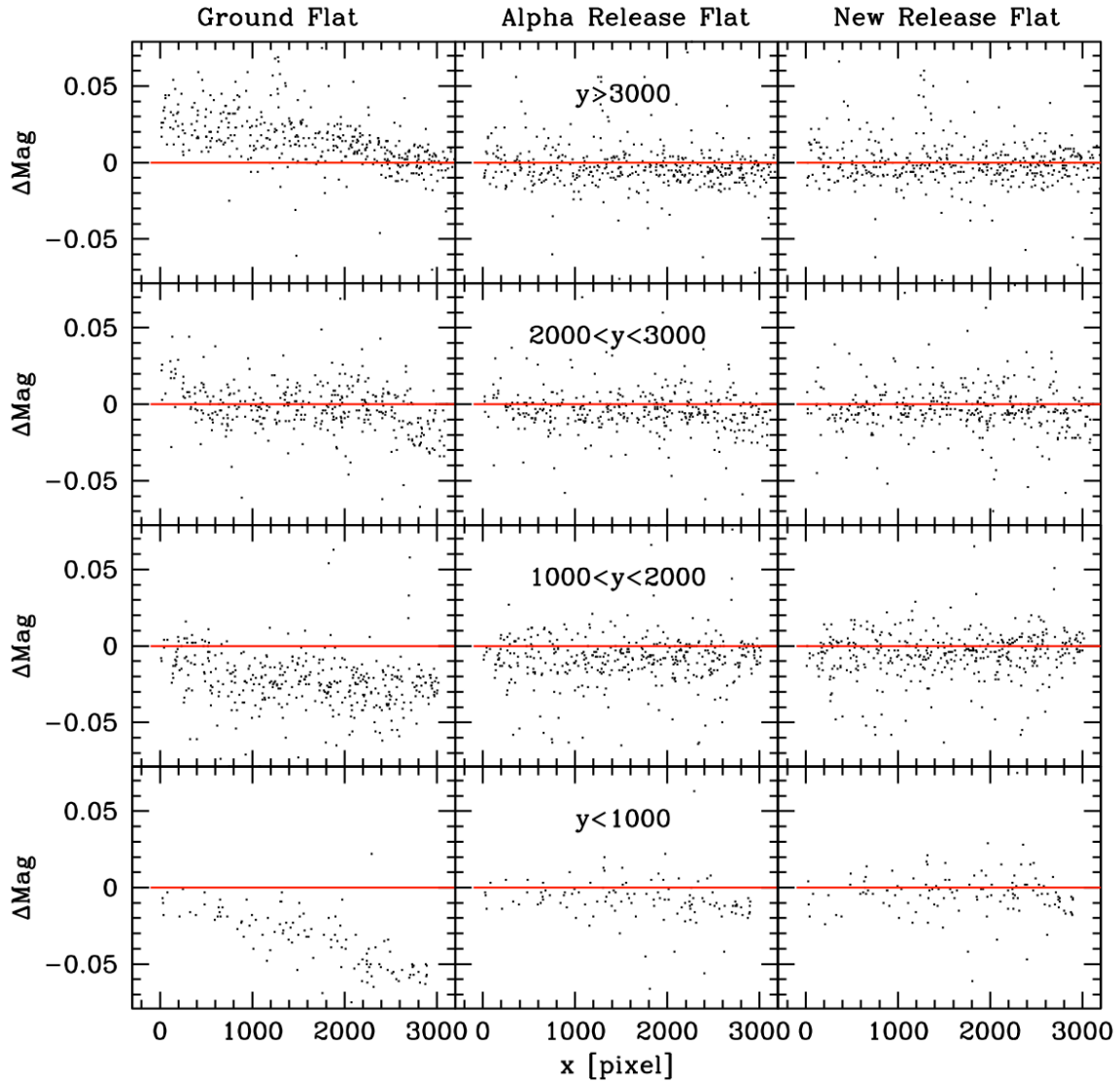


Figure 14: Difference in the apparent magnitude for stars in the magnitude range $16.0 < m_{F814W} < 19.5$ (with photometric errors less than $\sim 0.1\%$) in two images of Omega Centauri acquired with a 185 degree roll. Relative photometry using a 5 pixel aperture is shown using the ground-based flats (left), the ‘alpha release’ flats (center) and the new flats, including an additional correction to $0.4''$ (right). The magnitude difference is plotted as a function of x-position for four separate regions selected by y-position. The red line represents zero difference and is shown to guide the eye.

11. Special Cases: The UV and Far-Red Filters

The Ultraviolet Filters

In order to obtain sufficient signal in the UV filters F218W, F225W, F275W and F280N, the CASTLE ground flats were obtained with the deuterium lamp in ambient conditions (-49C), rather than under vacuum conditions at the expected flight temperature (-82C). Differences in the UV flat field response due to temperature were expected, and the plan was to correct sensitivity residuals using on-orbit data.

Because flat fields are normalized to unity in UVIS1, the sensitivity differences between the two CCDs are apparent in the lower panel of Figure 15, adapted from Sabbi et al. (2009). This figure plots the normalized count rate for each chip in the three broadband UV filters F218W, F225W, and F275W. Note that in the ultraviolet, UVIS2 achieves higher sensitivity than UVIS1, and this difference increases toward shorter wavelengths.

For these ultraviolet filters, a crosshatch pattern due to detection-layer structure in the CCDs is visible in both chips. Ground test data in the F336W filter include flat fields obtained with the xenon lamp at both -49C (ambient) and -82C (vacuum), presented in Figure 16. The ratio of these flats shows a residual crosshatch pattern of $\pm 2\text{-}3\%$ peak to peak. Similar temperature-dependent residual structure is expected for the ambient deuterium lamp flats, and calibration observations in cycles 19 and 20 (programs 12707 and 13096) will help model the strength of the crosshatch residuals in F225W and F275W by stepping a spectrophotometric standard across the detector. A second calibration program will spatially scan a pair of stars back and forth across the detector to constrain the strength of the residuals. We hope that at least one of these two techniques will provide enough information to model and correct for the residual pattern.

The crosshatch pattern cannot be removed by the L-flat algorithm which is designed to model only low-frequency structure. Residual QE offsets between chips, however, *will* be removed since the L-flat solution for each detector grid point is determined as a unique solution. While no clear chip-dependent offset is apparent in the F275W L-flat (Figure 11), a possible offset is suspected in F225W. Scaling the mean value of the UVIS1 L-flat up by 1.5%, the shape of the F225W L-flat begins to resemble the F275W L-flat solution, especially in blue/purple region in the upper left corner of the detector where the residuals are largest. This similar shape is expected if the UV L-flat solutions are wavelength dependent, as found for the optical wavelength broadband filters. The dependence of any chip-dependent QE on spectral type is beyond this study, but is currently being investigated by observing spectrophotometric standards with a large range of colors on both UVIS chips (see Section 12 for details).

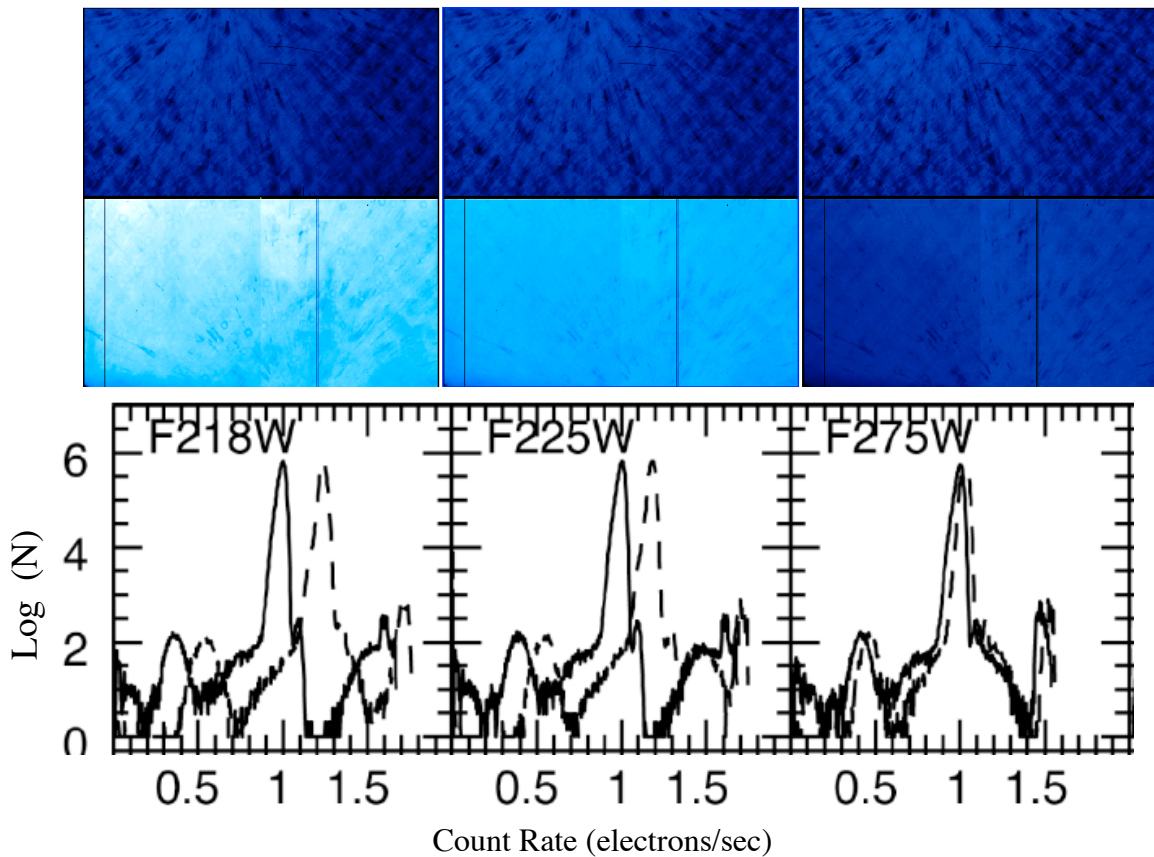


Figure 15: (Top) CASTLE LP-flats for three of the four UV filters obtained in ambient conditions at -49C . (Bottom) Count rates for UVIS1 (solid) and UVIS2 (dashed) from Sabbi et al. 2009 after normalization of the flat fields to 1.0 in UVIS1. Note that the QE offset between chips increases towards shorter wavelengths.

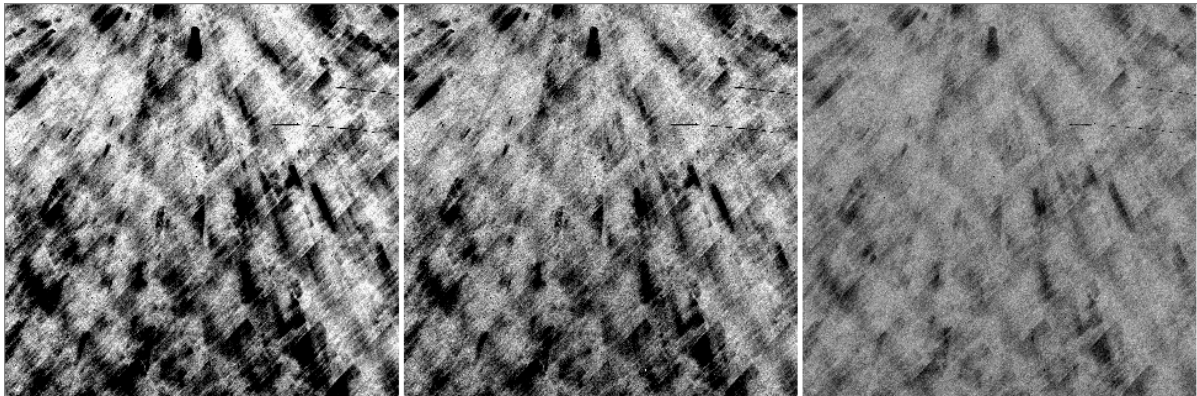


Figure 16: A subsection of the F336W ground flats acquired at -82C (left) and -49C (center) during TV3 testing. The ratio image (right) shows a residual crosshatch pattern similar to that expected for the F218W, F225W, F275W, and F280N filters. In the greyscale plot, black (white) corresponds to values less than (greater than) 1.0.

The Far-Red Filter, F850LP

The F850LP filter is part of the Sloan Digital Sky Survey filter set and is the reddest of the ultra-wide filters designed to provide high throughput for their specific wavelength range. At wavelengths approaching ~ 1 micron, the CCD's silicon becomes relatively transparent so that the glue adhering the detector to its package becomes visible (Brown 2007). The F850LP flat fields obtained during TV3 testing are presented in Figure 17, where the sensitivity in the dark regions of the 'piano key' glue pattern are approximately 1% lower than the surrounding regions. The panel at left shows the TV3 flat field obtained with CASTLE using the QTH Mirror VISIR (external) optical stimulus. The central panel shows the internal tungsten lamp flat. The ratio of the two (right) shows that the vertical glue bands are sensitive to the different color of the stimulus with residuals of 0.5-1.0%.

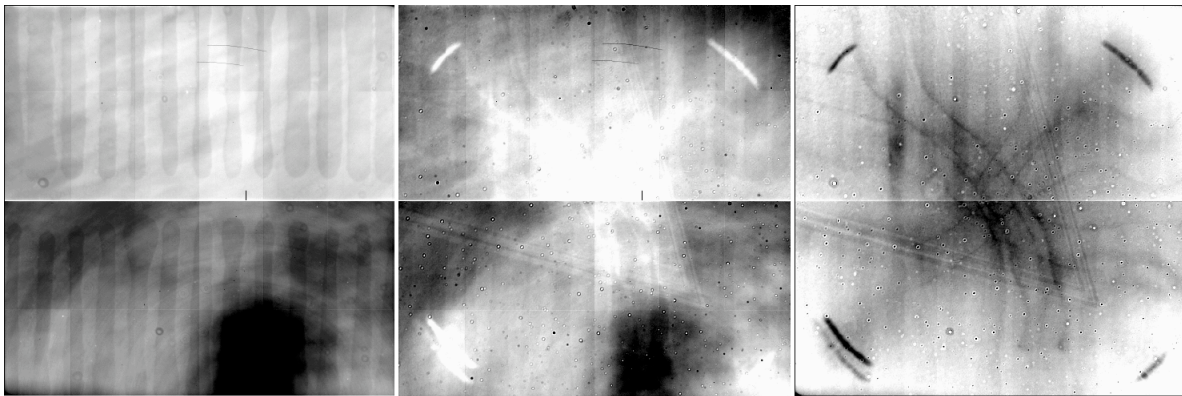


Figure 17: (Left) F850LP LP-flat obtained in TV3 with CASTLE using the QTH Mirror VISIR stimulus. Dark features are representative of low QE in the flat field. (Center) Internal lamp flat obtained during TV3 with the tungsten lamp. (Right) Ratio image, showing the effect of the color of the optical stimulus on the flat. Note that the vertical 'glue' features correspond to residual vertical bands at the level of ~ 0.5 -1.0%.

The high order L-flat solution derived from the Omega Centauri cluster observations also shows vertical residuals. Figure 18 presents the 32x32, 16x16, and 8x8 pixel grid solutions. Since the cluster stars are significantly bluer than the calibration lamps (which resemble a 10,000K blackbody), the glue features in the LP-flats show up as $\sim 1\%$ vertical residuals when the 32x32 L-flat grid lines up precisely with one of these features. To average out this effect, a lower order solution (16x16) was used for F850LP. Observers using this filter are advised that errors at the 1% level are expected for sources that are significantly bluer than the CASTLE stimulus.

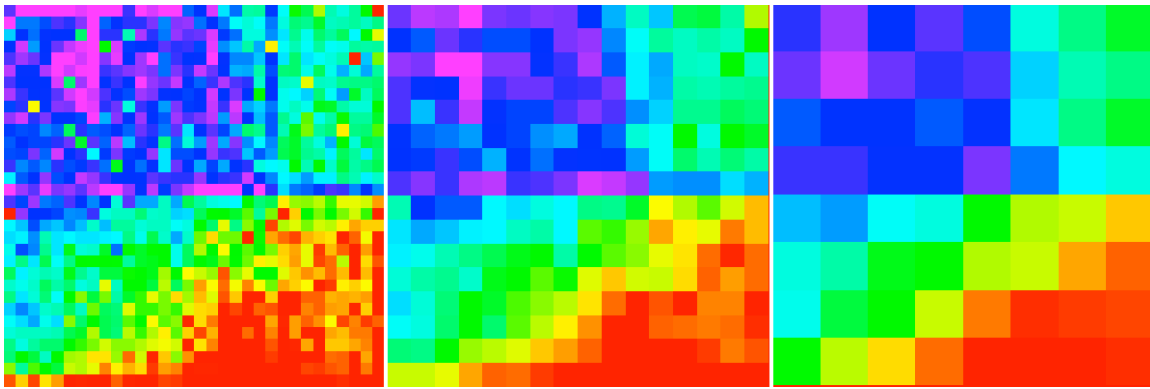


Figure 18: The F850LP L-flat solution represented as a 32x32 grid (left), a 16x16 grid (center) and 8x8 grid (right). Since the cluster stars are significantly bluer than the calibration lamps, glue features in the LP-flats show up as ~1% vertical residuals in the 32x32 grid solution. To approximately average out this effect, the 16x6 grid solution was used instead to correct the F850LP ground flats.

12. UVIS Zeropoints

Because QE differences between UVIS1 and UVIS2 are accounted for in the flat field (see Section 2), users need only apply a single zeropoint value when performing photometry of both chips using calibrated, flat fielded (flt.fits) or drizzled (drz.fits) images. CALWF3 uses SYNPHOT to populate the photometric keywords in the calibrated image header but is capable of handling both raw and flat fielded data. In the HST Exposure Time Calculators, observers use the combined throughput for an observation mode by multiplying the individual throughputs of the components in the optical path to determine total counts or signal-to-noise ratios when planning observations. However, observers may also use SYNPHOT to interpret their calibrated (flat fielded) data post-execution. Because the flat field reference files correct for the differences in QE between the chips, a “cal” keyword switch has been provided in SYNPHOT for the UVIS detector (Brown 2008b). For example, if observers wish to predict the signal-to-noise for a star observed in the F336W filter on UVIS2, one would specify “wfc3, uvis2, f336w” as the observation mode. If, however, observers wish to predict the countrate in flat fielded data, one would specify “wfc3, uvis2, f336w, cal” as the observation mode. The former gives the inverse sensitivity PHOTFLAM of $1.27\text{e-}18 \text{ erg cm}^{-2} \text{ sec}^{-1} \text{ \AA}^{-1}$. The later gives a value of $1.31\text{e-}18 \text{ erg cm}^{-2} \text{ sec}^{-1} \text{ \AA}^{-1}$, a 3% difference due to the flat field median value being equal to 0.97 rather than 1.0. When the additional ‘cal’ switch is used, the PHOTFLAM value of the two chips (and thus the photometric zeropoints) should be equal. Without it, the inherent QE response of the two chips is evident in the SYNPHOT results.

Further study is underway to characterize differences in color terms between the individual chips. For example, in Cycle 18 calibration program 12334 (UVIS & IR Photometric Zeropoints, PI: Kalirai), an expanded set of spectrophotometric standards were selected to span a range of spectral type and temperatures, including several A dwarfs, G dwarfs, and M and late-type dwarfs, in addition to the usual sample of hot white dwarf standards. These observations are intended to quantify differences in the computed zeropoints as a function of chip and of spectral type.

Conclusions

Flat fields for 42 UVIS filters were revised on December 14, 2011. Any data retrieved from MAST after this date will be calibrated with these new reference files. Alternately, the new flat fields may be obtained from the Calibration Database System (CDBS): <http://www.stsci.edu/hst/observatory/cdb/SIfileInfo/WFC3/WFC3PFLbin1UVIS>

The new UVIS flat fields are a combination of the flats obtained during ground testing and two separate corrections: a large wedge-shaped internal reflection and a residual low-frequency correction (L-flat) due to differences in the ground and in-flight flat fields. The wedge-shaped flare has been removed from the ground flats using a geometric model of the four ghost reflections. Low-frequency sensitivity residuals were computed in flight using high signal-to-noise observations of stars in Omega Centauri in 10 broadband filters. Aperture photometry for each image was corrected to an 0.4" aperture using a spatially-dependent aperture correction. The remaining 32 UVIS filters were corrected via interpolation based on the filter pivot wavelength.

Additional calibration in Cycles 19 & 20 will help validate the accuracy of these solutions. These include program 12706 (UVIS Window Ghosts, PI: Mack) which will measure the relative strength of the window ghosts as a function of wavelength. Programs 12707 (UVIS Spatial Stability, PI: Rajan) & 13096 (UVIS Flat Field Validation, PI: Mack) will verify the accuracy of the new flats by stepping a spectrophotometric standard across the detector in several additional filters, including F225W, F275W, F438W, F606W, and F814W. Programs 12713 (Spatial Scanned L-flat, PI: McCullough) and 13095 (UVIS L-Flat via Spatial Scans, PI: McCullough) will validate the accuracy of new flat fields by spatially scanning a pair of stars back and forth across the detector in the F225W, F275W, and F606W filters.

Late-breaking news on the UVIS flat fields, including future enhancements, will be documented on the WFC3 page: http://www.stsci.edu/hst/wfc3/analysis/uvis_flats

Acknowledgements

The authors would like to thank Peter McCullough for reviewing this ISR and providing helpful feedback. We are also grateful to Peter for sharing his model of the UVIS flare for removal from the ground flats. We thank Jay Anderson for providing access to his matching algorithms which allowed the creation of matched source catalogs. We are grateful to Andrea Bellini for sharing his spatially variable PSF-fitting code for UVIS which allowed the calculation of aperture corrections for each image. We thank Jason Kalirai, Tom Brown, and Susana Deustua for useful discussions on the interplay between the flat fields and zeropoints in the WFC3 calibration pipeline and in SYNPHOT. We are grateful to Abhijith Rajan for providing his early results of spatial repeatability of the F336W flat field. We also thank Vera Kozhurina-Platais for helpful discussions about the UVIS geometric distortion.

References

- Anderson, J., Bedin, L. R., Piotto, G., Yadav, R. S., & Bellini, A. 2006, *A&A*, 454, 1029
- Bellini, A. & Bedin, L. R. 2009, *PASP*, 121, 1419
- Brown, T. & Lupie, O. 2004, WFC3 ISR 2004-04, “Filter Ghosts in the WFC3 UVIS Channel”
- Brown, T. 2007a, WFC3 ISR 2007-21, “WFC3 TV2 Testing: UVIS Channel Glint”
- Brown, T. 2007b, WFC3 ISR 2007-24, “WFC3 TV2 Testing: UVIS Filtered Throughput”
- Brown, T., Hartig, G., & Baggett, S. 2008, WFC3 ISR 2008-10, “WFC3 TV3 Testing: UVIS Window Contamination”
- Brown, T. 2008a, WFC3 ISR 2008-07, “WFC3 TV3 Testing: UVIS Channel Glints”
- Brown, T. 2008b, WFC3 ISR 2008-48, “WFC3 TV3 Testing: System Throughput on the UVIS Build 1’ Detector”
- Bushouse, H. 2005, WFC3 ISR 2005-21, “WFC3 Thermal Vacuum Testing: UVIS Broadband Flat Fields”
- Dahlen, T., Mack, J. & Sabbi, E. 2013, WFC3 ISR 2013-xx, “A Full Set of UVIS Flat Fields using Interpolated Inflight Corrections”, in preparation
- Dressel, L. 2012, WFC3 ISR 2012-14, “Breathing, Position Drift, and PSF Variations on the UVIS Detector”
- Fruchter, A. S. & Hook, R. N. 2002, *PASP* 114, 144
- Kalirai, J., et al. 2009, WFC3 ISR 2009-31, “WFC3 SMOV Proposal 11450: The Photometric Performance and Calibration of WFC3/UVIS”
- Kalirai, J. S., Cox, C., Dressel, L., Fruchter, A., Hack, W., Kozhurina-Platais, V., & Mack, J. 2010, WFC3 ISR 2010-08, “WFC3 Pixel Area Maps”
- Laidler et al, 2008, “Synphot Data User’s Guide” (Baltimore, STScI)
- Mack, J., Bohlin, R.C., Gilliland, R., van der Marel, R., Blakeslee, J., & de Marchi, G. 2002, ACS ISR 2002-08, “ACS L-Flats for the WFC”
- Mack, J., Bohlin, R.C., Gilliland, R., van der Marel, R. 2005a, in “The 2005 HST Calibration Workshop”, ed. A. M. Koekemoer, P. Goudfrooij, and L. L. Dressel (Baltimore: STScI), 67, “ACS Flat Field Update and New SBC L-flats”

Mack, J., Gilliland, R., van der Marel, R., & Bohlin, R.C. 2005b, ACS ISR 2005-13, “SBC L-Flat Corrections and Time-Dependent Sensitivity”

van der Marel, R. 2003, ACS ISR 2003-10 , “Determination of Low-Frequency Flat- Field Structure from Photometry of Stellar Fields”

McCullough, P. 2011, WFC3 ISR 2011-16 , “Geometric model of UVIS window ghosts in WFC3”

Pirzkal, N., Mack, J., Dahlen, T., & Sabbi, E. 2011, WFC3 ISR 2011-11, “Sky Flats: Generating Improved WFC3 IR Flat-fields”

Rajan, A., Mack J., Kalirai, J., Sabbi, E., & Deustua, S. 2013, WFC3 ISR 2013-xx, “Spatial Photometric Stability of the WFC3/UVIS Channel”, in preparation

Sabbi, E. 2008, WFC3 ISR 2008-12, “UVIS CASTLE Photometric Filter Flat Field Atlas”

Sabbi, E., Dulude, M., Martel, A.R., Baggett, S., & Bushouse, H. 2009, WFC3 ISR 2008-46, “WFC3 Ground P-flats”

Sabbi, E. 2009, WFC3 ISR 2009-19, “WFC3 SMOV Program 11452: UVIS Flat Field Uniformity”

Sabbi, E., Dulude, M., Martel, A.R., Baggett, S., & Bushouse, H. 2009, WFC3 ISR 2008-46, “WFC3 UVIS Ground P-flats”

Sabbi, E. & Bellini, A. 2013, WFC3 ISR-2013-xx, “UVIS PSF Spatial and Temporal Variations”, in preparation

Stiavelli, M., Sullivan, J., & Flemming, J. 2001, WFC3 ISR 2001-17, “Modeling the Impact of Ghosts in WFC3/UVIS”

Wong, M. 2010, in “The 2010 STScI Calibration Workshop”, ed. S. Deustua and C. Oliveira (Baltimore: STScI), 183, “Fringing in the WFC3/UVIS Detector”